Demonstration of ensemble data assimilation for Mars using DART, MarsWRF, and radiance observations from MGS TES

C. Lee,[1] W. G. Lawson,[2] M. I. Richardson,[1] J. L. Anderson,[3] N. Collins,[3] T. Hoar,[3] and M. Mischna[4]

Received 10 February 2011; revised 8 August 2011; accepted 19 August 2011; published 29 November 2011.

[1] We describe a global atmospheric data assimilation scheme that has been adapted for use with a Martian General Circulation Model (GCM), with the ultimate goal of creating globally and temporally interpolated "reanalysis" data sets from planetary atmospheric observations. The system uses the Data Assimilation Research Testbed (DART) software to apply an Ensemble Kalman Filter (EnKF) to the MarsWRF GCM. Specific application to Mars also required the development of a radiance forward model for near-nadir Thermal Emission Spectrometer (TES) observations. Preliminary results from an assimilation of 40 sols of TES radiance data, taken around $L_s = 150°$ (August 1999, Mars Year 24), are provided. 1.3 million TES observations are ingested and used to improve the state prediction by the GCM, with bias and error reductions obtained throughout the state vector. Results from the assimilation suggest steepening of the latitudinal and vertical thermal gradients with concurrent strengthening of the mid-latitude zonal jets, and a slower recession of the southern polar ice edge than predicted by the unaided GCM. Limitations of the prescribed dust model are highlighted by the presence of an atmospheric radiance bias. Preliminary results suggest the prescribed dust vertical profile might not be suitable for all seasons, in accordance with more recent observations of the vertical distribution of dust by the Mars Climate Sounder. The tools developed using this DA system are available at http://www.marsclimatecenter.com. A tutorial and example TES radiance assimilation are also provided.

Citation: Lee, C., W. G. Lawson, M. I. Richardson, J. L. Anderson, N. Collins, T. Hoar, and M. Mischna (2011), Demonstration of ensemble data assimilation for Mars using DART, MarsWRF, and radiance observations from MGS TES, *J. Geophys. Res.*, *116*, E11011, doi:10.1029/2011JE003815.

1. Introduction

[2] Data assimilation (DA) is the popular term in geophysical fluid dynamics for problems of combining the information content in observations and models. In the context of the Martian atmosphere, data assimilation is the process of combining remote observations of the Martian atmosphere with General Circulation Models (GCMs) to produce a self-consistent description of the state and evolution of the Martian atmosphere. Over the past decade observations by the NASA Mars Global Surveyor (MGS), Mars Reconnaissance Orbiter (MRO), and ESA Mars Express have provided a wealth of data with which to constrain GCMs using data assimilation and multiple DA systems are being developed to utilize this information in the context of climate modeling and weather forecasting (e.g., this work, *Hoffman et al.* [2010b], and *Moudden and Forbes* [2010]).

[3] In order to ingest observations into a GCM we require a method that allows us to objectively compare model predictions with observations while accounting for the inherent error in both processes. One such method is the Kalman filter [*Kalman*, 1960; *Kalman and Bucy*, 1961], where the model prediction and observation are combined in the context of a Bayesian algorithm to determine the most likely state given the available information.

[4] This paper describes the application of a variation of the Kalman filter (the Ensemble Kalman filter) [e.g., *Evensen*, 1994, 2009; *Kalnay*, 2009] that can be applied to problems with a large number of degrees of freedom, such as those found in atmospheric sciences. Using a framework developed for generalized data assimilation problems, the Data Assimilation Research Testbed [*Anderson et al.*, 2009], we will assimilate the radiance observations made by the Thermal Emission Spectrometer (TES) [*Christensen et al.*, 2001] aboard the MGS satellite. These radiance observations will be directly ingested within the DA system using a forward model to simulate the observations using the information on atmospheric temperature, pressure and

[1]Ashima Research, Pasadena, California, USA.
[2]Point Carbon, Washington, D. C., USA.
[3]Institute for Mathematics Applied to Geosciences, National Center for Atmospheric Research, Boulder, Colorado, USA.
[4]Jet Propulsion Laboratory, California Institute of Technology, Pasadena, California, USA.

0148-0227/11/2011JE003815

opacity contained in the Martian GCM (MarsWRF) [*Richardson et al.*, 2007]. While the assimilation of calibrated radiance data is novel in Martian data assimilation, the benefits obtained from assimilating temperature retrievals in the study of the Martian atmosphere have been shown in previous work [e.g., *Banfield et al.*, 1995; *Houben*, 1999; *Lewis and Read*, 1995]. In terrestrial data assimilation, the direct assimilation of calibrated radiances [*Eyre et al.*, 1993; *Andersson et al.*, 1994] has produced noticeable improvements over the assimilation of temperatures retrieved from those same radiances.

[5] Early approaches to Martian data assimilation made a number of simplifying approximations that allowed rapid development of the DA systems while providing significant improvements to the simulations. Many of these approximations had also been made in terrestrial data assimilation, and were intended to reduce the complexity of problem to a manageable level considering the computational resources available. For example, *Houben* [1999] used a truncated state space Mars atmosphere model (effectively a reduced resolution and complexity GCM) with a 4D variational data assimilation method, where a model adjoint is used to determine the corrections that are applied to the model state in order to match the available observations. Extensive validated results have yet to be published from this study.

[6] Another simplifying approximation, made by *Banfield et al.* [1995], was to assume that the relationship between model variables would remain constant in time. This assumption implies a constant (in time) covariance between elements in the model state vector that allows a steady-state Kalman filter to be used [e.g., *Kalnay*, 2002]. In this approach, the results from an ensemble of GCM instantiations are used to derive the covariance matrix that is then used to correct the unobserved variables in the model state (e.g. winds) after deriving suitable corrections to the observed variables (e.g. temperature). *Banfield et al.* [1995] reported some success with this method, but suggested that assimilation of aerosols would be necessary for further improvement of their results.

[7] *Lewis et al.* [2007] use a once-operational terrestrial assimilation scheme, the Analysis Correction Scheme [*Lorenc et al.*, 1991], where observations are used to construct a corrective forcing that is then applied to the model prognostic variables within the GCM. This approach is successful in the sense that it generates a time sequence of analyzed model states and has been validated using independent data sets with reasonable success [*Montabone et al.*, 2006]. However, the ad-hoc nature of the applied forcing makes longer-term corrections of the model state difficult.

[8] A more advanced, time dependent, Local Ensemble Transform Kalman Filter (LETKF) has been implemented by *Hoffman et al.* [2010b] in order to assimilate atmospheric temperatures derived from radiance observations from TES. In this approach, an ensemble of GCM instantiations are maintained to derive the time-dependent covariance matrix used to determine the corrections to the GCM state. This method has been used to run Observing System Simulation Experiments (OSSE) where one instantiation of the GCM is used as truth and the remainder of the ensemble attempts to simulate this truth. Assimilations with real TES retrieved temperatures are ongoing and *Hoffman et al.* [2010a] have found that applying a bias correction to the model state reduces the biases in their assimilation and allows for better comparison with the available observations.

[9] The work we describe here is an ongoing effort to develop an ensemble Data Assimilation (DA) system for the Martian atmosphere that is flexible with regard to the components used. We have developed our DA system using the Data Assimilation Research Testbed (DART) [*Anderson et al.*, 2009], a rigorous and expandable framework that allows various observation types and models to be combined using a common interface to an Ensemble Kalman Filter or Smoother. To perform data assimilation with DART, we use the MarsWRF GCM [*Richardson et al.*, 2007], a global version of the Weather, Research and Forecast model developed at NCAR for terrestrial mesoscale simulation (WRF) [*Skamarock and Klemp*, 2008].

[10] We use the DA system to ingest near Infra-Red (IR) radiance observations taken by the TES instrument aboard the MGS satellite. We use a forward model to simulate radiance observations of the Martian atmosphere that can be compared directly with the calibrated radiances stored in the TES database [*Christensen et al.*, 2001]. The use of a radiances in our assimilation, rather than retrieved temperature data [e.g., *Hoffman et al.*, 2010b] significantly reduces the amount of numerical processing we perform on each observation before assimilation. This allows us to retain more of the information available in each observation. For example, each radiance observation contains information on the thermal structure, aerosol distribution, and surface properties. Using information from the GCM, we can simulate this radiance observation in a consistent manner, rather than using the dust distribution or surface properties assumed by the retrieval team.

[11] The remainder of this manuscript describes the components used in the DA system, and presents preliminary results from a short assimilation of TES radiances. In section 2 we describe each component of the DA system, beginning with the GCM, MarsWRF, followed by the TES radiance forward model, and the DART model interface, and finally the observation pre-processing required. In section 3 we show the results from a 40 sol TES radiance assimilation near $L_s = 150°$. In section 4 we perform three additional experiments using the same TES data after excluding dust and/or surface properties from the state vector to gauge their effect on the assimilation. Finally, in section 5 we provide a summary of our results and our conclusions.

2. Data Assimilation System

[12] The data assimilation approach we use is based on an Ensemble Kalman filter (EnKF), where we evolve an ensemble of N slightly differing model states that each attempt to simulate the Martian atmosphere. Each ensemble member has an associated state vector that holds the variables being modified by the DA. The state vector for MarsWRF contains surface and atmospheric temperature, surface and atmospheric pressure, surface albedo and emissivity, surface CO_2 ice, column dust opacity, and the horizontal wind vector. Additional assimilations omitting surface albedo or emissivity from the state vector have also been performed and will be discussed later.

[13] This ensemble is used to provide a prediction of the atmospheric state (represented by the ensemble mean) and to

provide necessary information on the variability of the atmosphere and covariance of the state vector (through the ensemble variance) [*Evensen*, 1994; *Evensen and VanLeeuwen*, 1996; *Anderson*, 2001]. This information is used, along with observations, within the Kalman filter to adjust the state of each ensemble member to more accurately simulate the atmosphere at the time of the observation, and to represent the uncertainty of the atmospheric state using the ensemble variance.

[14] We perform an iterated cycle of forecast integration and assimilation. The integration step is performed by the MarsWRF GCM under the control of the DART software, which maintains the ensemble of model states and provides the initial conditions necessary to continue the simulation. The assimilation step is performed by the DART software. In the assimilation step we compare observations with forward model simulated radiances to derive a correction to the ensemble in observation space (the innovation), that is consequently applied to the ensemble states using the derived covariance matrix. In this section we will describe each component as they relate to the DA system. More detailed descriptions of each component, including validation and experimental results, can be found in the referenced literature.

2.1. The Mars Weather Research and Forecast Model

[15] We use version 3.0.1.1 of the MarsWRF climate model [*Richardson et al.*, 2007]. We prescribe the radiative forcing in the GCM using a two stream, single scattering, radiative flux solver based on the Hadley Centre Unified Model algorithm [*Edwards and Slingo*, 1996], modified by *Mischna et al.* [2006] for use in MarsWRF. This parameterization calculates fluxes in the visible and infra-red spectra using a correlated-k method to specify the optical properties of the carbon dioxide atmosphere, and Mie scattering derived parameters to describe the radiative effects of the atmospheric dust and water.

[16] MarsWRF simulates well the climatological mean state of the Martian atmosphere, including the seasonal CO_2 cycle [*Guo et al.*, 2009] and the spatial and temporal structure of the dominant atmospheric thermal tides [*Lee et al.*, 2009]. Investigation of the water ice cycle [*Inada et al.*, 2005; *Mischna et al.*, 2005], active dust cycle [*Newman et al.*, 2006], and paleo-climate [*Mischna et al.*, 2005; *Soto and Richardson*, 2009; A. Soto et al., Global constraints on precipitation and aridity on ancient Mars, submitted to *Journal of Geophysical Research*, 2011] are ongoing with the global version of MarsWRF.

[17] The surface visible albedo, surface IR emissivity, and column dust opacity parameterizations have been modified from the nominal MarsWRF GCM [*Richardson et al.*, 2007] to facilitate the data assimilation process. In the nominal MarsWRF GCM the surface visible albedo and surface IR emissivity are prescribed fields (based on results from TES observations [*Christensen et al.*, 2001; *Bandfield*, 2002]), with modification due only to deposition of CO_2 ice on the surface whose albedo and emissivity are also prescribed [*Guo et al.*, 2009]. Within the DA system, we allow both the albedo and emissivity to be modified by the DA system independently of any changes to the CO_2 ice, dust loading, or other surface properties. This allows the DA system to simulate mixed surface types by smoothly varying surface properties between the prescribed extrema (e.g. dust covered ice or partial ice covered grid boxes) that are not simulated in the nominal GCM.

[18] The column dust opacity is modified in a similar way. The nominal dust parameterization is based on the 'MGS' scenario used in the Mars Climate Database [*Lewis et al.*, 1999], which uses a vertically prescribed relative dust profile and additionally prescribes the spatial and temporal variability of the column dust opacity. Within the DA system, we update the column dust opacity to agree with the nominal model by injecting or removing dust, but we also allow the DA system to modify the column dust opacity as necessary. We do not allow the DA system to modify the vertical profile of the dust column from the modified *Conrath* [1975] profile. Recent work reported by *Heavens et al.* [2011a, 2011b] suggests that the dust distribution in the Martian atmosphere is not well represented by a Conrath-like profile at all seasons. Ongoing work with MarsWRF includes the implementation of an advected dust scheme within the DA system that should improve the representation of dust in our model.

[19] The observations we use from TES are linked to observation times based on the J2000 ephemeris system. To ingest these observations accurately in time and space we use the Mars24 timing scheme [*Allison and McEwan*, 2000] within MarsWRF. The Mars24 system allows us to calculate the true local solar time and heliocentric longitude (L_s) given the information available in the TES database, which in turn allows us to place the TES observations correctly within the simulated atmosphere (e.g. accounting for variable sol length). This modification corrects two possible errors; First, the mean solar time (i.e. assuming a fixed solar day length) deviates from the true solar time by up to 90 minutes over a year; Second, each year $L_s = 0°$ corresponds to a different local time at the prime meridian (due to the non-integer number of sols in each year).

2.2. Observation Forward Model

[20] At each assimilation step we use an observation forward model within the DA system to simulate the observations using the state vectors of the ensemble members. In the radiance assimilation we perform, the observations simulated are the calibrated radiances observed using TES [*Christensen et al.*, 2001] aboard the Mars Global Surveyor (MGS), and the observation forward model used to simulate the observation is a two-stream single-scattering radiative transfer model.

[21] TES is a nadir sounding grating spectrometer, observing from 200 to 1700 cm^{-1} with a resolution of 5.29 cm^{-1} or 10.58 cm^{-1} depending on the scan mode. These data can be obtained from the NASA Planetary Data System archive (PDS, http://pds.jpl.nasa.gov). We consider 24 high resolution radiance bands between 572 cm^{-1} and 815 cm^{-1} within the DA system, capturing radiance from the surface and atmosphere up-to approximately 35 km altitude. In our current verification and validation tests of the DA system, and in the plots shown here, we use radiance data from detector 2 with no detector mask applied.

[22] To ingest the calibrated radiance data from TES we use a custom radiance forward model developed using a two–stream flux solver [*Edwards and Slingo*, 1996] based on the radiation parameterization used within MarsWRF to simulate the infra-red and solar fluxes in the GCM

[*Johnson et al.*, 2008]. The forward model calculates Top-Of-Atmosphere (TOA) fluxes from the atmosphere at a resolution of 5.29 cm^{-1} using pre-calculated correlated-k tables [*Lacis and Oinas*, 1989] and the prescribed dust parameters used within the model [*Wolff and Clancy*, 2003], ensuring consistency between the two radiation models. The calculated TOA fluxes are convolved with a truncated sinc function to represent the Instrument Line Shape to fully simulate an observation by TES. The Full Width at Half-Maximum (FWHM) of the sinc function is set to the resolution for TES, 6.72 cm^{-1} for the high resolution scans used here. We truncate this calculation at (the spectral bin containing) 1 FWHM, giving 3 points of calculation at high resolution and 5 points at low resolution.

2.3. DART Assimilation and Innovation

[23] Once the observations have been simulated at a single assimilation time (i.e. the prior has been calculated) the ensemble of model states, including the simulated observations, is used to calculate the terms of the covariance matrix that will be used to apply corrections to all of the fields based on corrections to the simulated observations. If necessary, variance inflation [*Anderson and Anderson*, 1999; *Anderson*, 2009] can be applied to the observation predictions to increase the simulated spread in the predictions, and covariance localization [*Houtekamer and Mitchell*, 2006] can be applied during the regression step used to transform the innovations back into state space. Using this data, the innovations to the simulated observations are calculated using a Bayesian algorithm, and the covariance matrix is used to propagate these corrections to the entire state vector. After the innovation has been applied, DART repeats the forward model calculation for every simulated observation, producing the posterior.

[24] The cycle of forecast integration and assimilation is repeated until the end of the assimilation, as determined by the availability of observations or constraints placed on the assimilation by the user.

2.4. Assimilation Setup and Procedure

[25] To perform an assimilation we begin with an instantiation of the MarsWRF model forced only with the internally described physical parameterizations and beginning from a rest state. This model is integrated as described by *Richardson et al.* [2007] for at least 1 Martian year to produce a statistically steady-state atmosphere. The integration of this model state ends 50 sols before the intended start of the assimilation.

[26] To create the ensemble of model states, the steady-state atmosphere is perturbed using additive Gaussian white noise perturbations on the temperature, surface pressure, horizontal wind, emissivity, albedo, and column dust opacity. Each ensemble member is then integrated for the remaining 50 sols to allow them to reach a new steady state. The magnitudes of the perturbations are small (e.g. standard deviations of 2 K in temperature, 5 m/s in horizontal wind, 0.02 in albedo and emissivity) and are constrained to keep albedo and emissivity between zero and one.

2.5. TES Observation Processing

[27] We minimally process the TES data to produce the input data set for use in the data assimilation. The processing includes calculating time and location data to place the observation correctly within the GCM, and gridding the data to improve the representativeness by producing a data set that is more comparable with the output of the GCM. Essentially, we are applying the smoothing function of the GCM (a spatial smoothing) to the TES data, just as we apply a spectral smoothing function (the Instrument Line Shape) to the GCM simulated radiances. This is analogous to the procedure used when comparing the retrieved data from two satellite observations [*Rodgers and Connor*, 2003], where the averaging kernel from each instrument is applied to the retrieved profiles from the other instrument, allowing more realistic comparison.

[28] The TES data is first processed using the vanilla tool to extract ephemeris data, location data, and radiance information. The ephemeris time is converted to a Mars Solar Day (the 'calendar' sol) and Mars Coordinated Time (the time at the Prime Meridian) for the observation, and the location data is used to place the observation on the surface of Mars. We group observations into co-located sets based on the model grid and on the ephemeris time of the observation, with each set containing all observations within each model grid box that are contiguous in time. Each observation set contains about 20 multi-band observations. Using these collated observations, we calculate a mean and variance of the set. The mean is used as the observed radiance, and the maximum of the variance and the instrument error [*Smith et al.*, 2001] is used as the observation error.

[29] Within the DA scheme, we assimilate new observations each hour there are suitable data — gaps in observations are integrated by the GCM, but no assimilation step occurs. We ingest all observations that occur within 30 minutes of the assimilation time at the assimilation time, after comparing with the acceptance criteria based on GCM and observation errors. Each observation is used in one assimilation step only and simulated once by the forward model for each ensemble member (for the Prior, and again for the Posterior). We do not attempt to better 'fit' the observation before the assimilation step. The only constraints placed upon the forward model input are those imposed by the GCM.

[30] For each TES observation we include information from the TES database (or derive from available data) the scan resolution, satellite zenith angle, heliocentric longitude, aerocentric longitude and latitude, Mars Solar Day (MSD), and Mars Coordinated Time. We use the wave number of the band center to represent the wave number of the observation, and we do not account for the very small differences in central wave number that occur in each of the six detectors. This data is sufficient, in concert with the GCM state vector, to allow the forward model to reproduce the observation.

[31] The data assimilation setup we have chosen is sufficiently flexible that ingesting alternate data requires only a suitable observation operator for that data. While we have tested TES retrieved temperature assimilation with DART, we have not included those results here because the preliminary assimilation lacked a suitable smoothing observation operator that would reduce the effective resolution of the GCM to the resolution of TES. This observation operator would perform a similar action to the smoothing applied by *Lewis et al.* [2007] to their GCM within the analysis correction scheme. Combined with a suitable dust

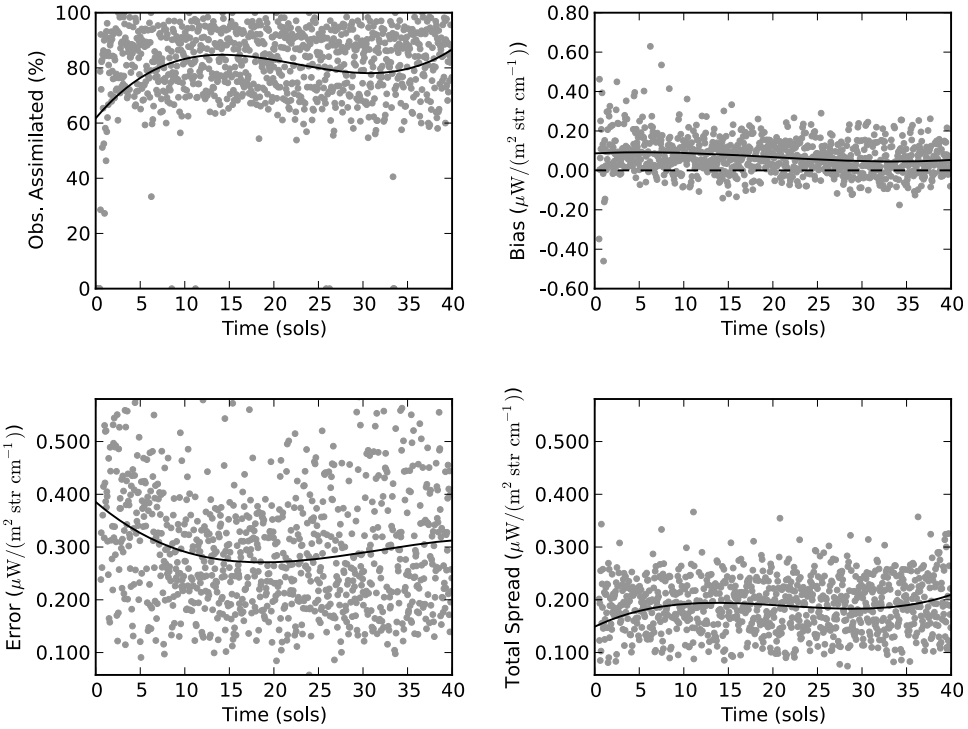

Figure 1. Results from the 40-sol assimilation of TES radiances, shown for the surface band at 572 cm^{-1}. Each plot shows the hourly binned data as grey dots, and the quartic fit through the data as a black line. The quartic fit is the least squares best quartic fit but not necessarily the least squares polynomial fit or best model for the data being fit. (top left) fraction of the available observations that were ingested during each assimilation period. (top right) Bias (Prior-Observation). (bottom left) RMS Error. (bottom right) Total Spread (standard deviation) of the 20-member ensemble and the observational error.

assimilation scheme this observation operator would allow us to assimilate the TES retrieved parameters without using calibrated radiances used here.

3. Results

[32] In this section we give an example of the DA system in operation. We will use a 20 member ensemble to assimilate 40 sols of TES radiance observations. These observations were taken between June and August 1999 (Mars Year 24, approximately L_s = 150° to L_s = 170°). We use 24 radiance bands from each of the 1.3 million TES spectra (from 572 to 815 cm^{-1}), and use this to define 30 million independent radiance observations. Using the method outlined in section 2.5, we collate this data to approximately 1.6 million gridded observations for use in the DA system. In the experiment shown here, we do not increase the spread of observations using observation inflation [*Anderson and Anderson*, 1999; *Anderson*, 2009]. Localization is applied using a *Gaspari and Cohn* [1999] function with a half-width of 10 degrees (about ~600 km). For every observation we ingest, DART calculates the prior and posterior in radiance observations, and the ensemble variances associated with each. From this data we can calculate a number of useful diagnostic fields, presented in Figures 1–5.

[33] Figure 1 shows four diagnostic fields for a single radiance band. For each observation we ingest, DART compares the observation with the prior ensemble and determines whether the observation should be ingested based on its difference from the prior ensemble mean. If the distance is smaller than a predefined threshold (3 times the square root of the sum of the prior and observational error variances) that observation is accepted, and this is shown in Figure 1 as the fraction of observations that are accepted and therefore used in the assimilation. If the GCM simulation is skillful we would expect a high fraction of observations to be accepted and the assimilation would improve the simulated atmosphere. Conversely, if a large fraction of the observations are rejected (due to low skill) there is a risk that the simulated atmosphere will deviate from reality. Figure 1 shows that we accept about 80% of the observations in this (surface) band, and in general we accept 75% of the observations. While this number is lower than we would like, it represents a large fraction of the available observations. Many of the rejections are due to biases in the model that are reduced by the assimilation and can be further reduced with improved physical parameterizations.

[34] Using all of the available observations, whether ingested or not, we can also measure the biases and errors in the ensemble. For example, in Figure 1 we calculate the bias and RMS error between the priors and the observations. We also show the spread of the ensemble members around the ensemble mean (in observation space, at the observation location). In this example, the RMS errors remain around 10^{-7} $W/m^2/str/cm^{-1}$, which corresponds to the minimum prescribed observational error, and the magnitude of the biases are reduced by the assimilation. However, the ensemble spread is small compared to the observation error in this

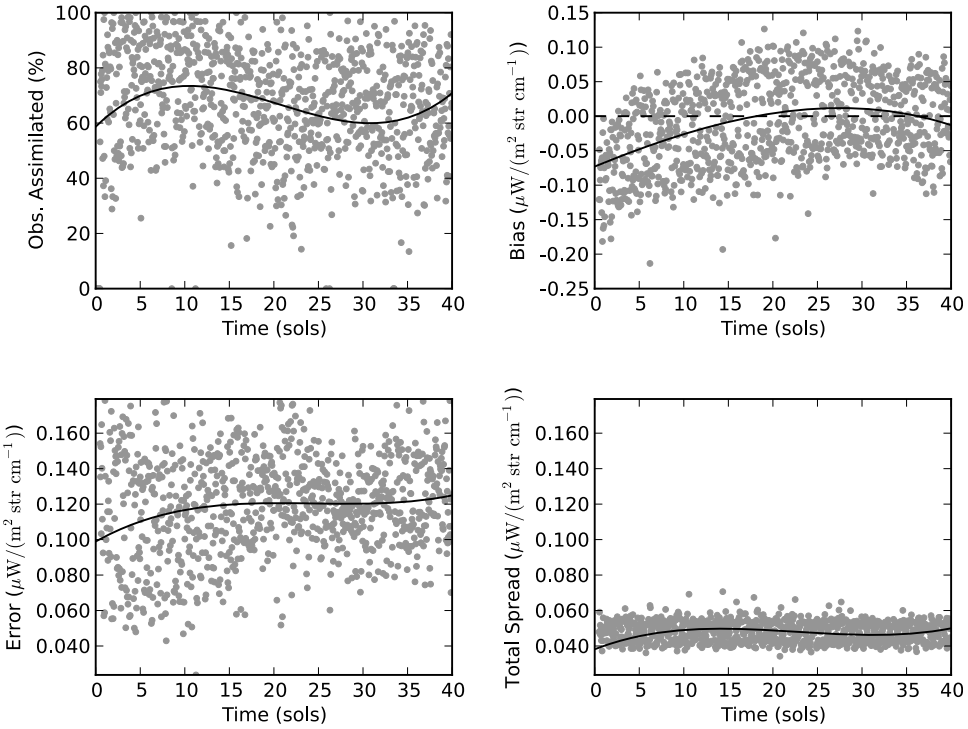

Figure 2. As Figure 1 but for the atmosphere band at 667 cm^{-1}.

band. That the Martian atmosphere has little variability is a known problem [*Newman et al.*, 2004] and there is some risk here that the ensemble could deviate significantly from reality and begin rejecting all observations, preventing any corrections to the state by the assimilation. In this example, the ensemble prediction is within the predefined error limits of 3 sigma for most of the observations and the climatology is a reasonably good estimate of the true atmosphere. As a result the ensemble does not deviate far from the true atmospheric state.

[35] Figure 1 shows the results from the 572 cm^{-1} band, dominated by radiance from the surface. Figure 2 shows the

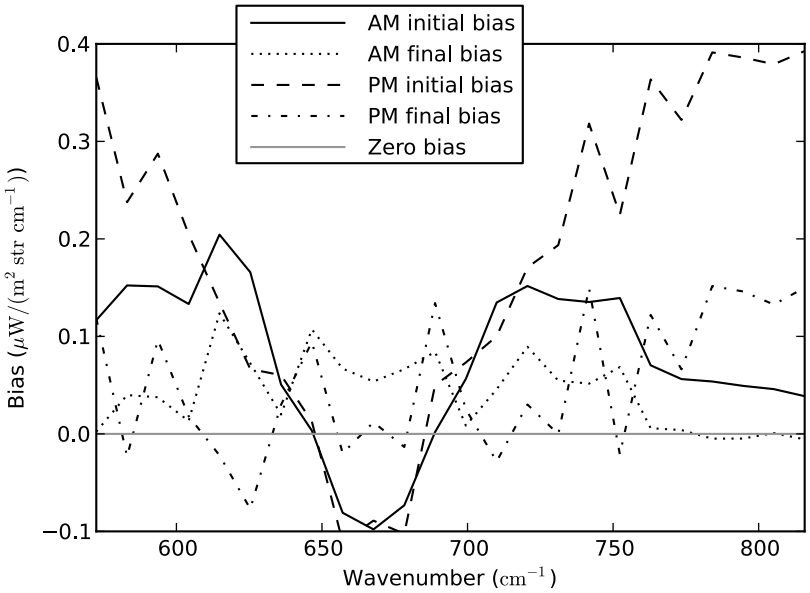

Figure 3. Biases for all bands separated into morning (AM) and afternoon (PM) observation times. The initial biases are Prior - Observation for the first sol of the assimilation. The final biases are Prior - Observation for the last sol of the assimilation. Bands below 620 cm^{-1} and above 720 cm^{-1} are dominated by radiance from the surface, while bands between 620 cm^{-1} and 720 cm^{-1} are dominated by radiance from the atmosphere.

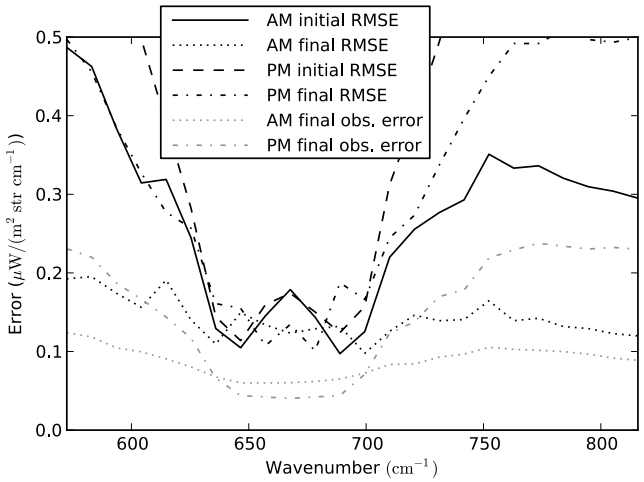

Figure 4. Total spread of the observation and ensemble states for all bands separated into morning (AM) and afternoon (PM) observation times.

same data from a radiance channel dominated by atmospheric temperature (667 cm^{-1}). The GCM typically performs better in simulating the surface radiance than the atmosphere dominated radiance, in part because the ensemble spread for the surface is larger than the atmosphere (relaxing the rejection criteria) but also because the surface dominated radiance is less sensitive to (parameterized) vertical profiles of aerosols than the atmosphere dominated radiances.

[36] In both the surface (Figure 1) and the atmosphere (Figure 2) bands the magnitude of the biases are reduced over the 40 sols, but with little change in the errors. In this example the RMS errors (bottom left) tend to be of the same magnitude as the Total Spread (total right), which suggests the ensemble is performing well during this season. Unreasonably large errors (i.e. much larger than the total spread) would imply a model error while unreasonably small errors (much smaller than the total spread)might suggest a GCM with insufficient physical constraints such that it can reproduce any observation including observational errors.

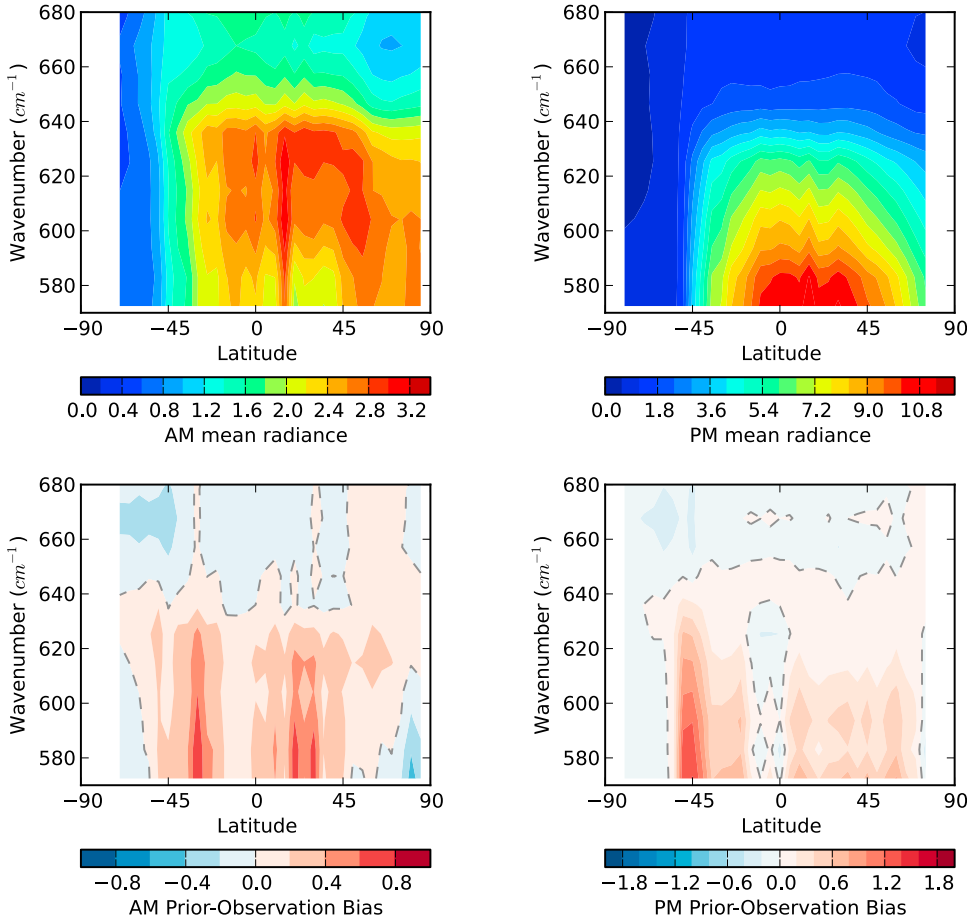

Figure 5. Longitudinal and time mean radiance (top) and observation-prior bias (bottom) for the morning (left) and afternoon (right) observation windows. Each figure shows the radiance and bias as a function of latitude (horizontal axis) and wave number (vertical axis). Only half of the ingested wave number range is shown and the wave number range shown is an approximate proxy for altitude, below 620 cm^{-1} corresponding to the surface, 680 cm^{-1} corresponding to a layer near 30 km altitude. In general, the morning observations are dominated by the warmer atmosphere, while afternoon observations are dominated by the warmer surface. The first sol of the assimilation is shown in this plot. All plots show radiance in μW/m^2/str/cm^{-1}.

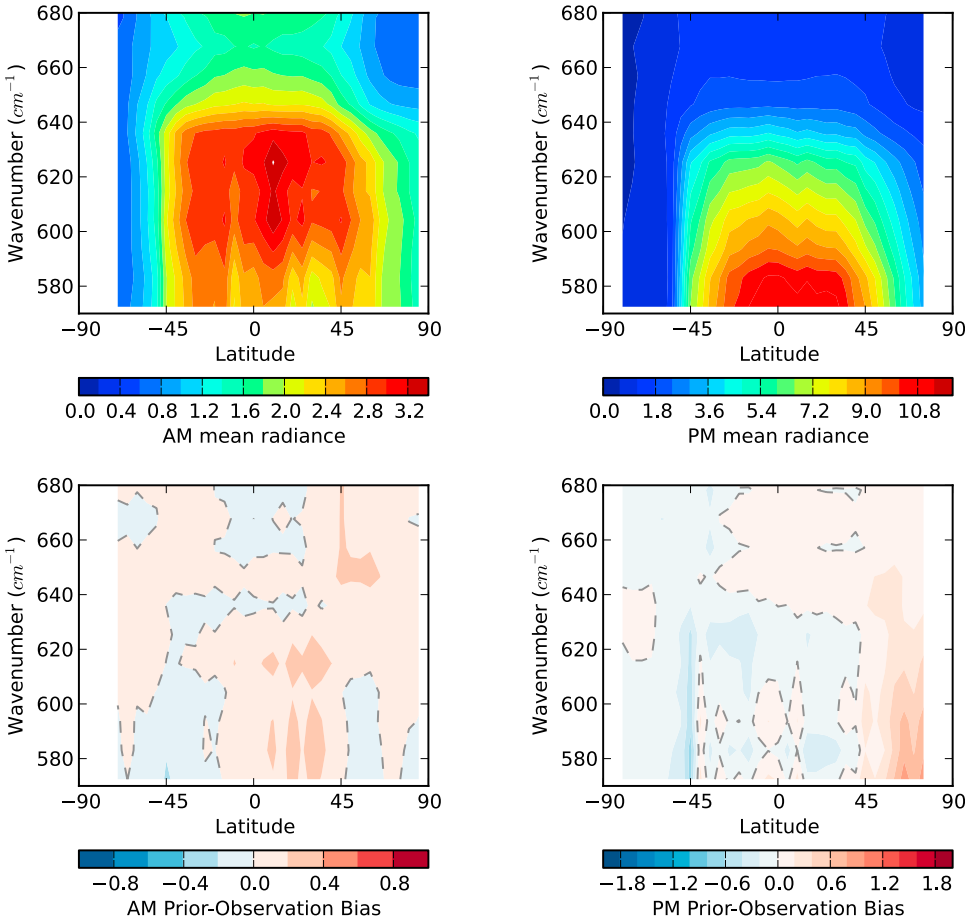

Figure 6. As Figure 5, but for the last sol of the assimilation.

[37] The trend in the acceptance percentage (top left in both figures) is best described by the trend in the bias field in Figure 2 (top right). The biases (and RMSE) are reduced in the first 10 sols of the assimilation, which a concurrent increase in the acceptance of observations. However, the corrections applied to the GCM eventually causes the biases to increase (for the surface) or overshoot (for the atmosphere) and result in an increase in the RMSE and concurrent decrease in acceptance rates. This oscillation should decrease in magnitude as the assimilation progresses.

[38] Figures 3 and 4 show the bias and RMS error, respectively, for all 24 bands, for the initial (0–1 sol) and final (39–40 sols) prior predictions. In general, the initial ensemble predicts a surface that is too bright (possibly too warm, too high emissivity or too low albedo, or too low column dust opacity) while the atmosphere tends to be slightly too dark (possibly too cold, or too much dust opacity). By the end of the assimilation, much of the bias in the surface field has been removed and the magnitude of the atmosphere biases have been reduced. However, in the process of correcting the biases in the surface the DA system has changed the sign of the bias in the atmosphere, and even increased the bias slightly in the lower atmosphere (e.g. at 640 cm^{-1} and 700 cm^{-1}). This is clearer in Figure 4, showing the RMS errors, where the lower atmosphere errors have increased while most other errors have decreased.

[39] One reason for the increase in RMS error in the lower atmosphere and sign change in the atmospheric bias is that the lower atmosphere is coupled to the surface and upper atmosphere by the fixed dust vertical profile. The assimilation is unable to alter the nature of this coupling by altering the vertical profile and the result is that while the assimilation improves the surface dominated radiances, the physical constraints within the GCM propagate these changes unnecessarily into the atmosphere.

[40] Using the same data set, Figures 5 and 6 separate the biases into the latitude bins used within the GCM (5 degrees wide from 90°S to 90°N), local time, and wave number bins as in Figures 3 and 4. Figure 5 shows the biases for the first sol, while Figure 6 shows the last sol, and we show only the lower half of the wave number range, from 572 cm^{-1} to 680 cm^{-1}, as a proxy for altitude. Radiance from below 620 cm^{-1} is essentially surface dominated radiance, while radiance from 667 cm^{-1} is dominated by the atmosphere at about 35 km.

[41] There are three large structural biases present in these figures. The first is the ice edge (at 45°S) where biases that are present at the start of the assimilation disappear by the end of the assimilation. The second bias is in the diurnal structure, where the GCM tends to under-predict the diurnal cycle at the surface and in the lower atmosphere. The third bias, in the vertical thermal lapse rate, is not clearly visible

in the observation (radiance) space, but can be seen in the temperature profile and will be discussed later.

[42] During the season we used in the assimilation, $L_s = 150°$ to $L_s = 170°$, the transient CO_2 ice over the southern polar region is sublimating as southern spring begins and the sub-solar latitude moves southward. In this simulation the GCM predicts an ice edge at 50°S, with soil to the north of this edge (with low albedo and high emissivity) and ice to the south (high albedo, low emissivity). However, the TES data suggest that the ice edge might be a few degrees north of the predicted ice edge, and this appears as a bright bias at the start of the assimilation. The ensemble predicts a warm surface, high emissivity, and low column dust opacity, all of which lead to a higher radiance from the surface. At the end of the assimilation, shown in Figure 6, the bias in the southern ice edge has reduced substantially, and in fact may be over-corrected which results in a small dark bias at the end of the assimilation.

[43] Near the end of the 40 sol assimilation, a bright bias appears in the northern hemisphere suggesting that the ensemble is missing the formation of the ice edge, or under-predicting the dust loading over the northern polar terminator. It is unlikely that ice forms in the northern mid-latitudes during this season though there may be a increase in column dust opacity at this time that is not simulated by the GCM.

[44] A different bias dominates the radiance from the ice-free surface (northward of 45°S). By separating the observations into day-time (2:00 PM to 4:00 PM) and night-time (2:00 AM to 4:00 AM) periods the biases that have a diurnal dependence can be seen (particularly near the equatorial surface). Neither albedo nor emissivity are expected to change significantly with the diurnal tide, leaving only column dust opacity or surface temperature as the cause of the bias. Thus, the ensemble either incorrectly predicts the amplitude of the surface temperature or atmospheric temperature response to solar tidal forcing, or the ensemble incorrectly parameterizes the response of column dust loading to solar tidal forcing. Although the assimilation attempts to remove dust, which would result in a larger diurnal thermal cycle that might remove this bias, the bias persists throughout the assimilation. This bias might be correctable by the assimilation given a better vertical dust profile, but the lack of change over the assimilation run suggests that a radiative component of the tropical atmosphere is missing. One possible component are the water ice clouds identified by *Wilson et al.* [2008] in the reanalysis data set produced by *Lewis et al.* [2007].

[45] We can also show the corrections to the ensemble state by comparing the thermal structure with the retrieved TES temperatures [*Smith et al.*, 2001]. These retrieved temperature profiles are given on constant pressure levels and are smoothed in altitude by the observation geometry and retrieval process. For this comparison we sampled the ensemble mean state at the time and location of each observation we assimilated. We then smoothed the sampled temperature profile output using the effective vertical resolution of TES given by *Eluskiewicz et al.* [2008] to produce a data set of simulated TES retrievals. This smoothing removes the variability in the vertical profile that TES cannot resolve, such as the inversion layer in the lower atmosphere, and produces smoother temperature profiles similar to those output by the retrieval process.

[46] We process the results from the nominal (i.e. not assimilated) and assimilation models in this way to create three similar data sets; The original TES data set, a simulated data set based on the nominal GCM ensemble, and a simulated data set based on the assimilation ensemble. These data sets are then gridded into 5 degree latitude bins and 1 sol time bins on the vertical levels used by the TES data set. Figures 7 and 8 show (from top to bottom) the TES retrieved temperatures, the mean difference between TES and the nominal GCM ensemble, and finally the difference between TES and the Prior ensemble mean from the assimilation. Both figures separate the morning (2:00 am–4:00 am) and afternoon (2:00 pm–4:00 pm) results, shown in the left and right columns, respectively.

[47] In the initial sol (Figure 7) both the nominal ensemble and assimilation ensemble predict a similar thermal structure, with small variations because of the effect of the assimilation during the first sol. Over most of the atmosphere there is a small bias in the vertical lapse rates, which dominate the afternoon biases. The GCM predicts a warmer boundary layer/lower atmosphere and colder middle atmosphere than suggested by TES observations, suggesting that the real atmosphere is more stable than the model prediction. Another bias occurs in the southern hemisphere near the ice edge and over the polar cap, where the GCM overpredicts the temperature and underpredicts the ice extent (as suggested earlier by the growth in the ice edge in the assimilation compared to nominal ensemble).

[48] At the end of the simulation (the last sol, Figure 8) the nominal GCM ensemble continues to overpredict the temperature in the northern mid-latitudes and the southern polar cap temperature but with smaller biases than the nominal ensemble. The assimilation is less successful in correcting the middle atmosphere than the near-surface atmosphere, because of the low variability in the ensemble and because of the constraints imposed by the fixed dust profile, which prevents the assimilation from changing the thermal lapse rate significantly.

[49] Many of the modifications to the state vector occur in the surface fields. Figure 9 shows the differences of surface fields and total column dust opacity between the ensemble and the nominal MarsWRF GCM (positive means a higher value in the assimilation ensemble in each case). For the surface fields we show the surface temperature, surface IR emissivity, and surface visible albedo. For the column dust opacity we show 7 mb dust opacity used within the GCM to define the column dust loading. In Figure 10, we show the prior minus observation radiance differences as before, gridded by latitude, local-time, and sol, for the surface band centered at 572 cm^{-1}.

[50] These figures, combined with Figures 5 and 6 show the evolution of the surface fields in response to the corrections derived from observations by the DA system. The ensemble initially predicts an ice edge near 50°S (shown in the emissivity and albedo fields) and as a result the surface brightness between 50°S and 45°S is overpredicted (Figure 5). Using the radiance observations, the DA system reduces this bias by increasing the ice-edge surface albedo (almost to the albedo of the ice-covered surface), increasing ice-covered

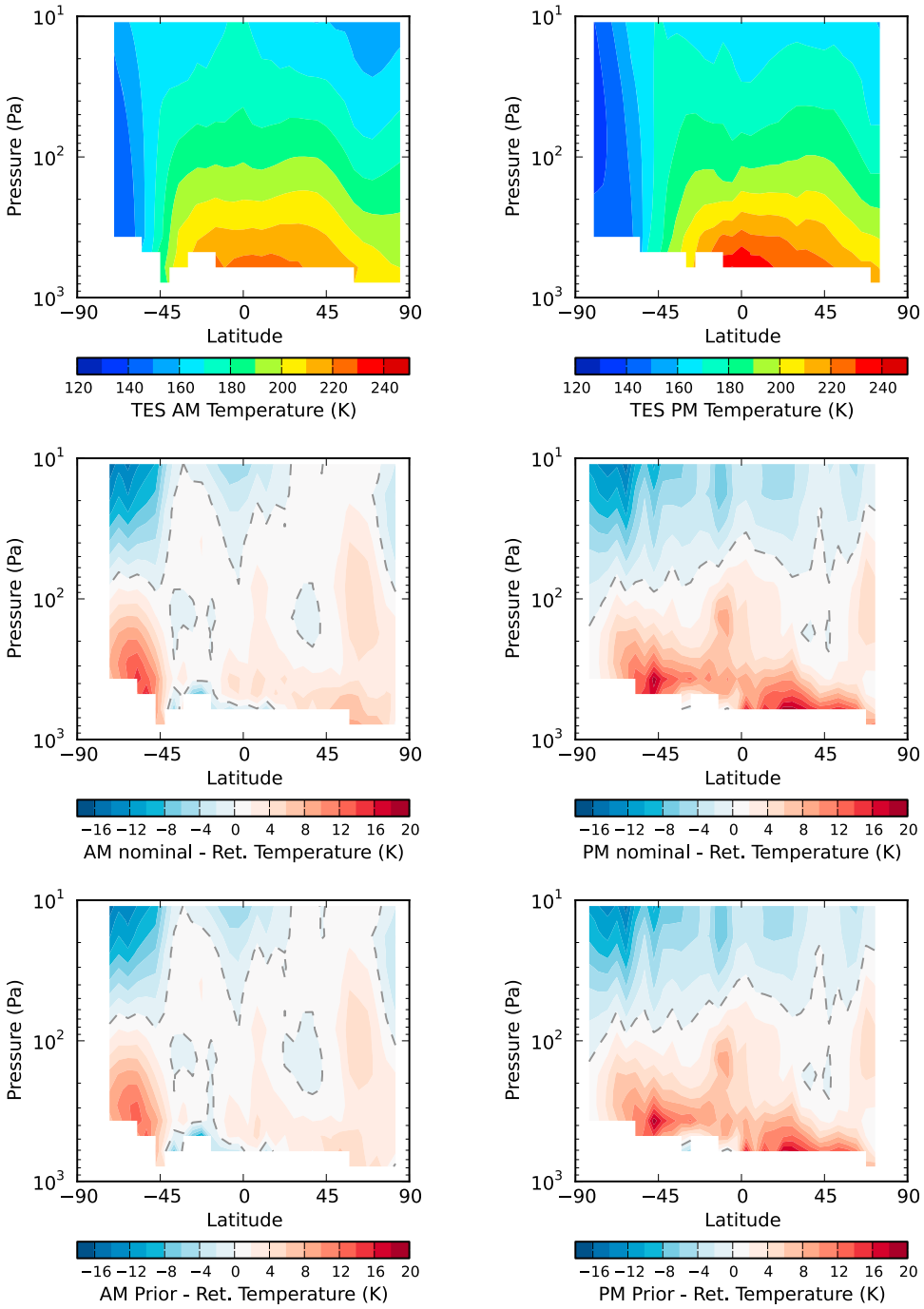

Figure 7. Longitudinal and time mean TES retrieved atmospheric temperature (top), nominal GCM-TES bias (middle), and assimilated GCM-TES bias (bottom), for the morning (left) and afternoon (right) observation windows. Each figure shows the temperature or bias as a function of latitude (horizontal axis) and pressure (vertical axis) between 1 kPa and 10 Pa. The first sol of the assimilation are shown in this plot. All plots show temperature in K.

emissivity, and increasing the column dust opacity along the ice-edge. As a result the surface temperature in this region drops about 15 K but remains above the CO_2 ice condensation temperature.

[51] The surface temperature predicted by the DA system is not unphysical, but it cannot be easily simulated in the nominal GCM where the surface parameterization of ice, albedo, and emissivity, are described using a binary model. The DA system produces a mixed state where, for example, the albedo is between that of the ice-free state and ice-covered state and the surface temperature is colder than the fully ice-free state predicted in the nominal model, but warmer than the fully ice-covered state. This result suggests that the surface parameterization could be refined to include

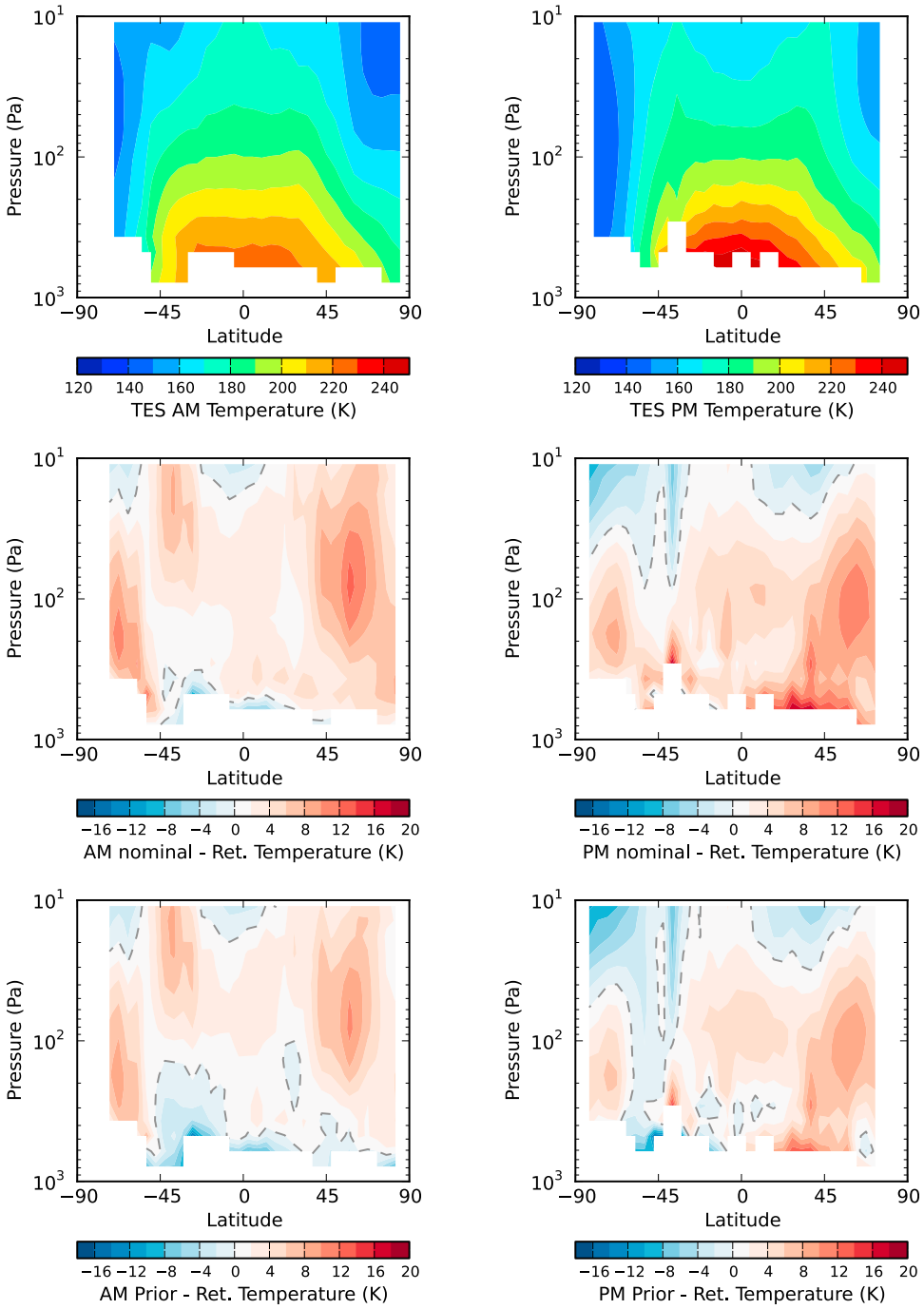

Figure 8. As Figure 7, but for the last sol of the assimilation.

fractional ice coverage, or multiple surface types within each grid box, which would help the forward model simulate the (grid-box average) observation more accurately. This type of sub-gridscale surface model is common in Earth GCMs [*Stensrud*, 2007] but rare in Martian GCMs.

[52] In the ice-free atmosphere, the observations suggest less dust in the summer tropics than in the nominal MarsWRF, and more dust near the northern polar terminator. The structure of the dust injection by the data assimilation suggests that the parameterized fixed dust field in MarsWRF tends to miss the dust lifting that occurs at the ice-edge and to a lesser extent at the polar terminator, and over-predicts the amount of long term dust in the atmosphere during this period (for this year). Recent work by *Cantor* [2007] and *Kahre et al.* [2010] suggests that much of the dust lifting should occur at the ice edge throughout the year, which is not captured by the current dust parameterization. A recent upgrade to the MarsWRF GCM includes an active, advected, three dimensional dust parameterization that will be used in future assimilations. This new dust parameterization is able to predict dust lifting on the surface, and should produce simulations more consistent

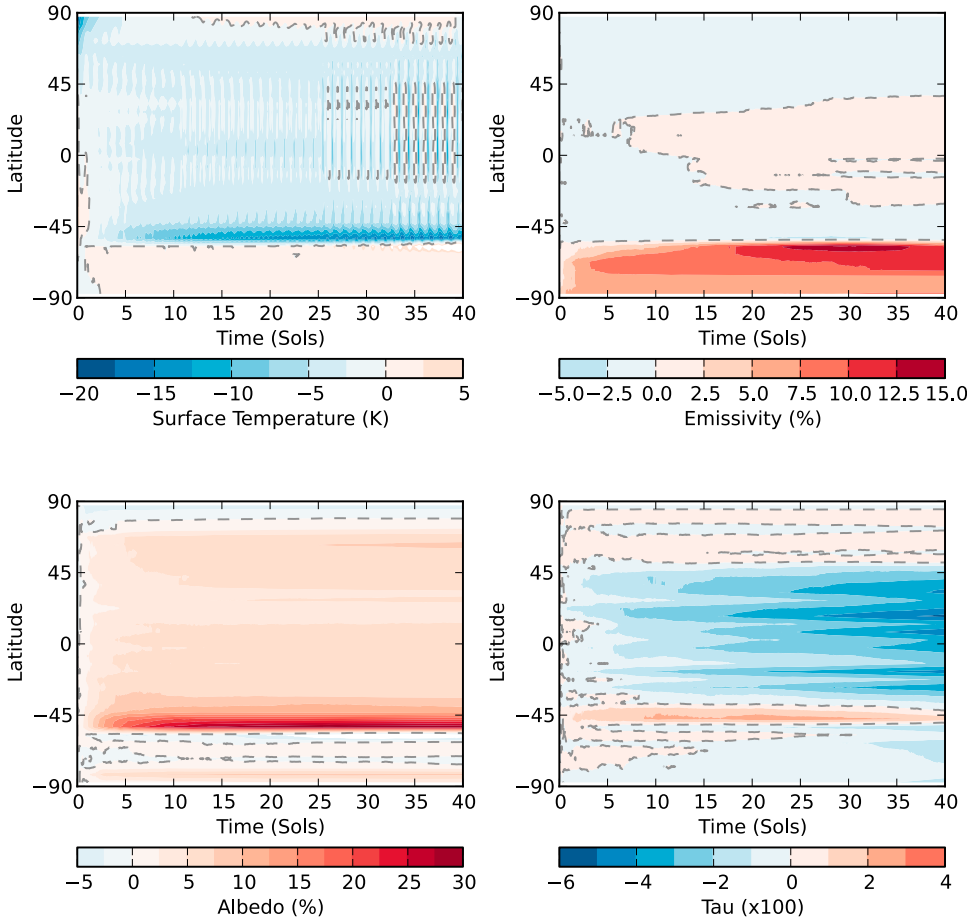

Figure 9. Longitudinally averaged difference between the assimilated model output and a nominal (not assimilated) model for the same time period. Top row, left-to-right: Surface temperature (K), Emissivity (%). Bottom row, left-to-right: Albedo (%), column dust opacity (0.01 opacity units).

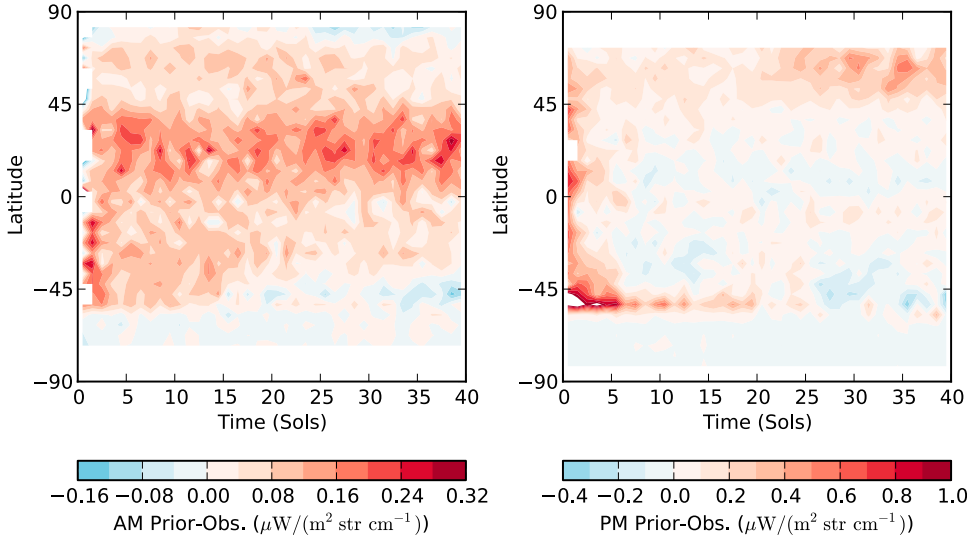

Figure 10. (left) Prior-Observation AM difference for a surface band in the assimilated model (μW/m^2/str/cm^{-1}), (right) Prior-Observation PM difference for a surface band (μW/m^2/str/cm^{-1}).

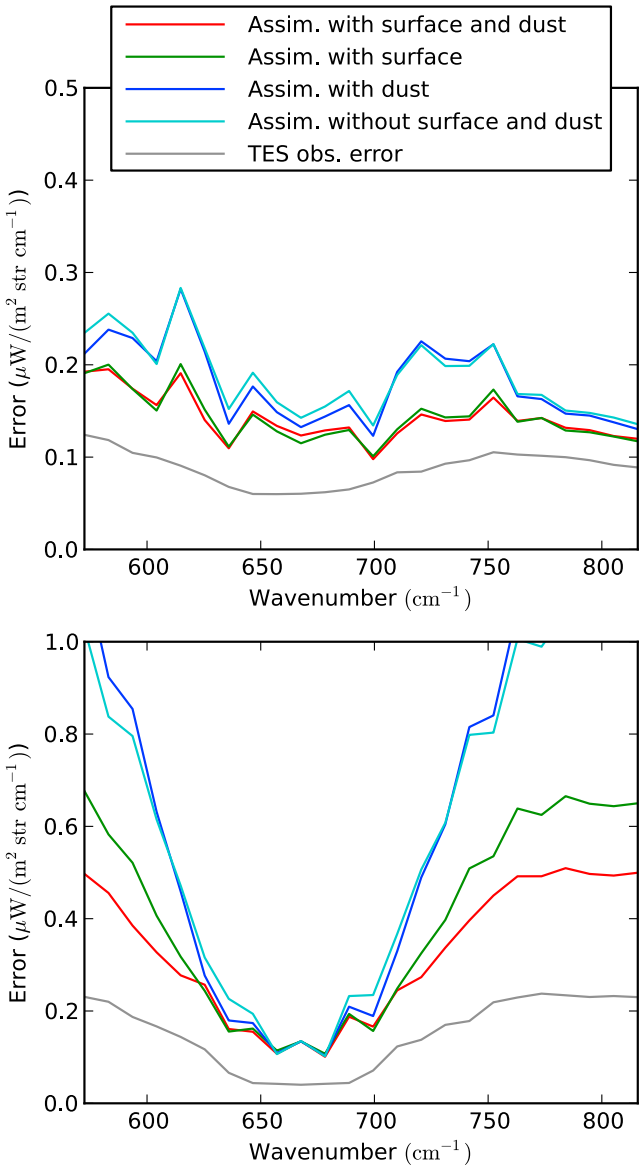

Figure 11. As Figure 4 for each of the assimilations discussed in section 4. (top) RMS Errors for the morning observations period of the final sol, (bottom) RMS Errors for the afternoon observations period of the final sol. (red) Assimilation with surface components and dust in the state vector, (green) assimilation with surface components, (blue) assimilation with dust but without surface components, (cyan) assimilation with neither surface nor dust components in the state vector, and (grey) the TES observational error for the last sol.

with the short term variability of dust loading in the observations.

4. Assimilation With Different State Vectors

[53] We conducted three further assimilation with the same input data set. The first assimilation, also discussed above, included dust, surface emissivity and surface albedo in the state vector (**a**: red in Figures 11 through 13). The second assimilation (**s**: green in the figures) excluded dust opacity (from the state vector, but not the GCM nor forward model) and kept the surface parameters, the third assimilation (**d**: blue in the figures) kept dust in the state vector but excluded emissivity and albedo, and the fourth assimilation (**f**) excluded dust, surface emissivity and surface albedo, keeping only the atmosphere components and the surface temperature and pressure. The latter three assimilations assume that our GCM uses the correct model for either dust opacity (**s**), surface properties (**d**), or both (**f**). Each assimilation used the same TES data set, but different initial ensembles to reflect the different state vector components (i.e. we do not perturb the dust opacity for the assimilation with no dust in the state vector).

[54] In general, the three new assimilations perform worse than the original assimilation. By far the worst assimilation is that with no dust or surface emissivity/albedo (**f**), which has very little effect on the lower atmospheric state. The percentage of observations we accept drops from 80%(**a**) to 60%(**f**) in the surface bands, and 75%(**a**) to 60%(**f**) in the atmosphere. The intermediate assimilations, (**s**) and (**d**), have intermediate acceptance percentages, varying in performance with spectral band. The assimilation with dust in the state vector(**d**) performs better in the lower and middle atmosphere, where dust is important, and the assimilation with surface parameters in the state vector(**s**) performs better at, and near, the surface.

[55] In the assimilation without both surface parameters and dust (**f**), the biases and errors are largest, with a larger overshoot in bias in the atmosphere bands (e.g. compared to sol 30 for assimilation (**a**) as shown in the top-right plot of Figure 1). In the (**f**) assimilation the biases and errors in the surface-dominated radiance fields are left largely uncorrected, errors in the lower atmosphere are actually worse, and errors in the upper atmosphere are comparable to the **a** assimilation. Figure 11 shows the final RMS errors as in Figure 4 for each of the assimilations, for the last sol, separated into morning (top) and afternoon (bottom) time periods. The morning results suggest one thing rather strongly, almost all of the error reduction comes from including the surface parameters in the state vector. The afternoon results are more nuanced, suggesting that the assimilations perform equally well in the middle atmosphere (radiances near 667 cm^{-1}), while the assimilation without surface properties (**d** and **f**) performs worse than the assimilations with surface properties (**a** and **s**) near the surface. Including dust (**d**) allows the lower and middle atmosphere to be corrected more effectively (reflected in the radiance errors between 620 cm^{-1} and 700 cm^{-1}), while independently including surface properties (**s**) allows the surface properties to be corrected and reduces surface radiance errors (below 620 cm^{-1} and above 700 cm^{-1}). Including dust and surface properties (**a**) performs the best of all, reducing the RMS errors more than the implied linear combination of corrections from the surface property (**s**) and dust (**d**) assimilations.

[56] Comparison with retrieved temperatures from TES (shown previously in Figures 7 and 8, not shown for the additional assimilations) again suggests that the assimilations performs comparably over the middle atmosphere while having differing impacts on the near surface temperature and particularly the ice-edge atmosphere. However, the trend remains the same, with (**a**) performing the best, and (**f**) performing the worst. Assimilation (**d**) has little effect

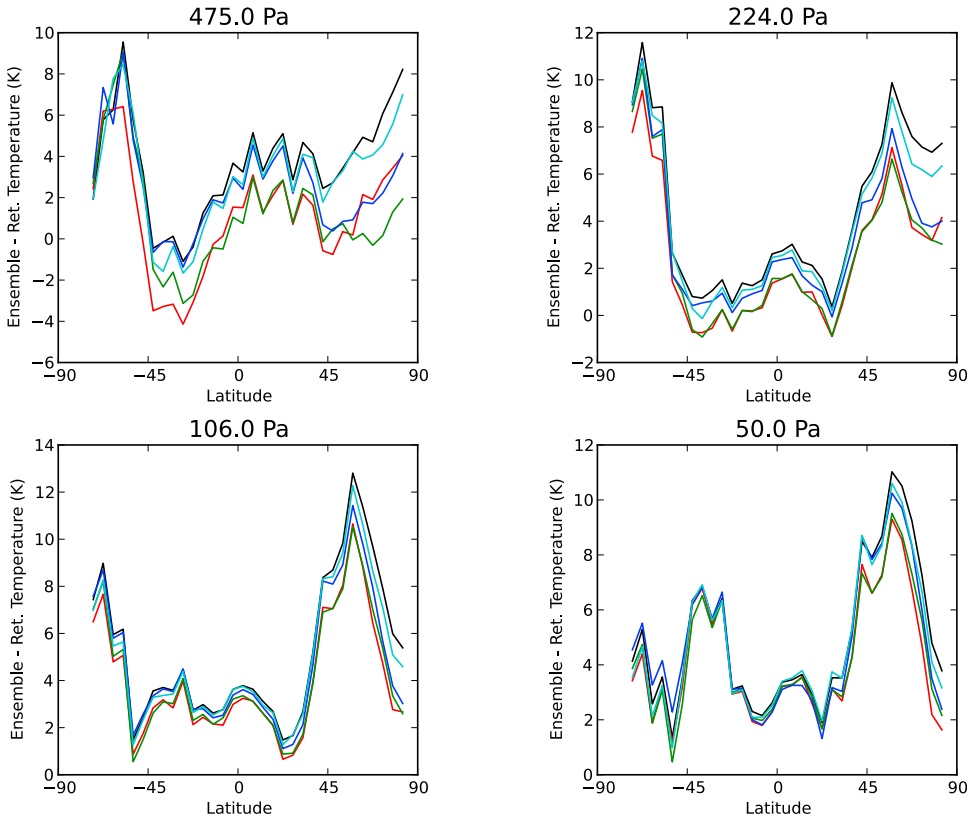

Figure 12. AM ensemble temperature minus TES retrieved temperature for the last sol of the assimilation. (black) nominal ensemble (no assimilation), (red) assimilation with surface components and dust in the state vector, (green) assimilation with surface components, (blue) assimilation with dust but without surface components, (cyan) assimilation with neither surface nor dust components in the state vector. Each plot is a single pressure level (top-left to bottom-right) at 475 Pa, 224 Pa, 106 Pa, 50 Pa. The cyan line follows the black line closely.

on the surface-dominated radiances, but corrects some of the temperature errors relative to TES retrievals and is comparable to the best assimilation (**a**) in the lower and middle atmosphere (where the model is most sensitive to dust). The (**s**) assimilation performs well in the lower atmosphere and in the surface fields,

[57] Figures 12 (morning) and 13 (afternoon) show summary plots for the four assimilation tests, showing ensemble mean temperature minus TES retrieved temperature for the last sol of the assimilations. Whether assimilated or not, the ensemble is generally warmer than TES data (as shown in earlier figures), and the corrections generally reduce the bias in temperatures by cooling the atmosphere. The assimilation with surface and dust components in the state vector is best designed to accomplish this, and the (**f**) assimilation with no dust nor surface properties in the state vector is again the worst. The effect is strongest in the lower atmosphere where these components have the greatest effect and where the warm bias is largest.

[58] In the upper atmosphere where the bias is less positive and sometimes negative, the difference between the assimilations is smaller. The apparent lack of correction is in part due to the over-confident ensemble producing extremely low variance in the (observable) radiances (e.g., Figure 2), but also because corrections in the lower atmosphere are propagated by the fixed dust profile to the upper atmosphere. This latter effect causes some errors to increase in the assimilations where the bias is already negative. For example, the southern hemisphere at 50 Pa (Figure 13) is cooled even though it is already too cold, because of the cooling of the lower atmosphere.

5. Summary and Conclusions

[59] We have developed an ensemble DA system to ingest calibrated radiance data from the TES [*Christensen et al.*, 2001] instrument aboard the MGS orbiter. The DA system uses DART [*Anderson et al.*, 2009] to drive the MarsWRF GCM [*Richardson et al.*, 2007], and a custom radiance forward model based on the MarsWRF internal radiation parameterization [*Mischna et al.*, 2006; *Johnson et al.*, 2008] to simulate the observations of the atmosphere made by TES.

[60] We tested this data assimilation system with a short integration of a 20 member ensemble using data from the start of the TES nominal mission, during July and August, 1999. We used approximately 1.6 million observations from the TES database to provide observations of the atmosphere over a 40 sol period (20 degrees of heliocentric longitude) starting at $L_s = 150°$.

[61] This assimilation test revealed three areas of the GCM that can be quickly improved to provide better simulation of the climatology and weather in the Martian

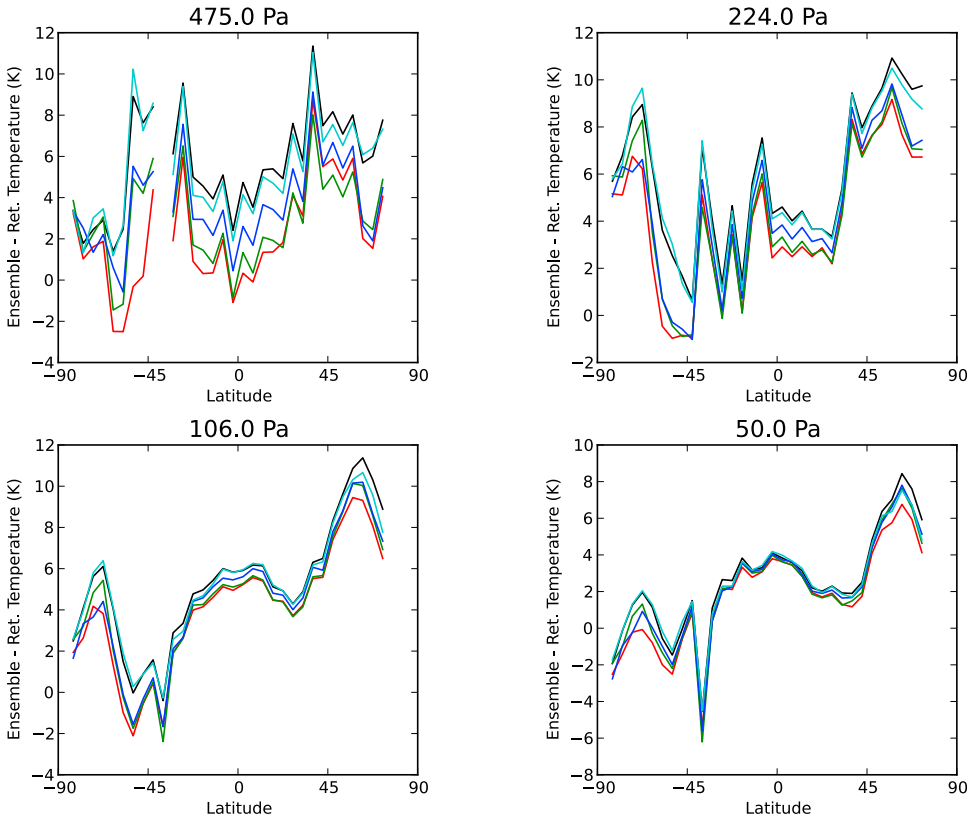

Figure 13. As Figure 12 but for the PM temperatures.

atmosphere. We found evidence that the MarsWRF under-predicts the latitudinal extent of the surface CO_2 ice during this season, resulting in a bright bias along the polar ice edge. One possible cause for this bias was identified in the column dust opacity over the polar ice-edge, where the observations (via the assimilation) suggested that we under-predict the column dust loading which might reduce the surface insolation and lower the temperature sufficiently to reduce the sublimation there.

[62] We also found that MarsWRF tends to under-predict the amplitude of the surface thermal response to the diurnal forcing. Separating the observations into morning (2:00 AM to 4:00 AM) and afternoon (2:00 PM to 4:00 PM) time periods highlighted a bright bias in the morning, and dark bias in the afternoon. These biases suggested a GCM diurnal tide response that is smaller than observed during this season. The apparent lack of reduction in this bias further suggested that a variable not controlled by the assimilation or present in the GCM is responsible, for example surface thermal properties or tropical ice clouds [*Wilson et al.*, 2008].

[63] As a test of our assimilation we compared the thermal structure predicted by the GCM ensemble with the temperature profiles retrieved from the TES observations we ingested. We found that the assimilation does improve the biases over the majority of the atmosphere, and especially near the ice-edge in the southern hemisphere and in the lower atmosphere. Additional tests where we limited the state vector to atmospheric properties produced worse results, and the assimilation was unable to correct the biases near ice edge. In particular, omitting the surface properties reduces the performance of the assimilation everywhere.

[64] The assimilation does not remove all model error. Our GCM, which is within the family of modern Martian GCMs [*Johnson et al.*, 2008], continues to exhibit some biases in its nominal state relative to the observed atmosphere. Much of this discrepancy appears due to incorrect parameters and models (e.g. the ice and dust lifting models discussed here) that can be improved with incremental changes, and more importantly progress is already being made in this area [e.g., *Kahre et al.*, 2010; *Greybush et al.*, 2011]. For example, we suggested that the lapse rate biases in the assimilation are caused in part by the fixed dust vertical profile that limits our ability to modify the thermal lapse rate in the lower atmosphere. More advanced dust models [*Newman et al.*, 2006] and parameterizations [*Heavens et al.*, 2011b] suggest different dust vertical profiles that might be more suitable than the one we used here [*Lewis et al.*, 1999].

[65] The biases we have found in the GCM suggest that it is not yet ready for operational forecasting of short term variability in the Martian atmosphere. This is equivalent to restating the findings from model inter-comparison studies that show current Mars GCM exhibit errors of order 10 K relative to zonal mean observations. However, it is clear that the data assimilation system as a whole is functioning successfully. We have shown that the assimilation can efficiently ingest radiance observations of the Martian atmosphere and surface, and that the assimilation improves the overall representation of the Martian atmosphere by our GCM. We have further shown that the assimilation of these observations provides explicit guidance on when and where the GCM lacks predictive skill, providing a crucial tool to help improve

our GCM, and hence improve our knowledge of the Martian climate system. Where possible, we should use these sparse observations to improve the underlying GCM rather than rely on empirical model corrections that appear to improve the assimilation while ultimately degrading the quality of long term re-analysis.

[66] The MarsWRF GCM and data assimilation interface described in this manuscript is available on the Mars Climate Center Web site (http://www.marsclimatecenter.com) and includes the tools necessary to use the MarsWRF GCM within the DA system, and the tools necessary to convert data from the TES database into suitable input files for use within the DA system. A subset of the TES data used in the example assimilation discussed in section 4 will also be provided as a tutorial on the DA system, and as a test case of the GCM and DA setup. DART will continue to be available from NCAR (http://www.image.ucar.edu/DAReS/DART/) and any modifications necessary to run the MarsWRF DA system and tutorial will be provided.

[67] Future work with this data assimilation system will be to perform a re-analysis of the Martian atmosphere using the radiance data from the TES instrument and the Mars Climate Sounder instrument (MCS) [*McCleese et al.*, 2007] on the Mars Reconnaissance Orbiter satellite. The data from TES and MCS will be used to create a near continuous record of the Martian atmosphere from 1999 to 2009 for use in the assimilation. As a limb sounder, MCS will offer improved vertical resolution and vertical coverage over TES but requires additional work to create a forward with limb sounding capabilities and to account for the increased sensitivity to scattering by dust and water ice.

[68] The results from this re-analysis will be used to create a gridded data set including the ensemble mean prediction and ensemble spread. This gridded data set will be released on the MarsWRF Web site and will be updated as new versions of the MarsWRF GCM are developed and improvements to the assimilation and forward model are made.

[69] **Acknowledgments.** This work was primarily funded by the NASA Applied Information Systems Research (AISR) Program under grant NNX09AN39G. Additional support was provided by the Mars Climate Sounder (MCS) project. We thank the three reviewers for their comments that have led to significant improvements in this manuscript.

References

Allison, M., and M. McEwan (2000), A post-Pathfinder evaluation of aerocentric solar coordinates with improved timing recipes for Mars seasonal/diurnal climate studies, *Planet. Space Sci.*, *48*, 215–235.

Anderson, J. L. (2001), An ensemble adjustment Kalman filter for data assimilation, *Mon. Weather Rev.*, *129*, 2884–2903.

Anderson, J. L. (2009), Spatially and temporally varying adaptive covariance inflation for ensemble filters, *Tellus, Ser. A*, *61*, 72–83.

Anderson, J. L., and S. L. Anderson (1999), A Monte Carlo implementation of the nonlinear filtering problem to produce ensemble assimilations and forecasts, *Mon. Weather Rev.*, *127*, 2741–2758.

Anderson, J. L., T. Hoar, K. Raeder, H. Liu, N. Collins, R. Torn, and A. Arellano (2009), The data assimilation research testbed: A community facility, *Bull. Am. Meteorol. Soc.*, *90*, 1283–1296.

Andersson, E., J. Pailleux, J. N. Thepaut, J. R. Eyre, A. P. McNally, G. A. Kelly, and P. Courtier (1994), Use of cloud-cleared radiances in three/four-dimensional variational data assimilation, *Q. J. R. Meteorol. Soc.*, *120*, 627–653.

Bandfield, J. L. (2002), Global mineral distributions on Mars, *J. Geophys. Res.*, *107*(E6), 5042, doi:10.1029/2001JE001510.

Banfield, D., A. P. Ingersoll, and C. L. Keppenne (1995), A steady-state Kalman filter for assimilating data from a single polar orbiting satellite, *J. Atmos. Sci.*, *52*(6), 737–753.

Cantor, B. A. (2007), MOC observations of the 2001 Mars planet-encircling dust storm, *Icarus*, *186*, 60–96.

Christensen, P. R., et al. (2001), Mars Global Surveyor Thermal Emission Spectrometer experiment: Investigation description and surface science results, *J. Geophys. Res.*, *106*(E10), 23,823–23,872.

Conrath, B. J. (1975), Thermal structure of the Martian atmosphere during the dissipation of the dust storm of 1971, *Icarus*, *24*(1), 36–46.

Edwards, J. M., and A. Slingo (1996), Studies with a flexible new radiation code: 1. Choosing a configuration for a large-scale model, *Q. J. R. Meteorol. Soc.*, *122*(531), 689–719.

Eluskiewicz, J., J.-L. Moncet, M. W. Shephard, K. Cady-Pereira, T. Connor, and G. Uymin (2008), Atmospheric and surface retrievals in the Mars polar regions from the Thermal Emission Spectrometer measurements, *J. Geophys. Res.*, *113*, E10010, doi:10.1029/2008JE003120.

Evensen, G. (1994), Sequential data assimilation with a nonlinear quasi-geostrophic model using montecarlo methods to forecast error statistics, *J. Geophys. Res.*, *99*, 10,143–10,162.

Evensen, G. (2009), *Data Assimilation: The Ensemble Kalman Filter*, 330 pp., Springer, Berlin.

Evensen, G., and P. J. VanLeeuwen (1996), Assimilation of GEOSAT altimeter data for the agulhas current using the ensemble Kalman filter with a quasigeostrophic model, *Mon. Weather Rev.*, *124*, 85–96.

Eyre, J. R., G. A. Kelly, A. P. McNally, E. Andersson, and A. Persson (1993), Assimilation of TOVS radiance information through one-dimensional variational analysis, *Q. J. R. Meteorol. Soc.*, *119*, 1427–1463.

Gaspari, G., and S. Cohn (1999), Construction of correlation functions in two and three dimensions. *Q. J. R. Meteorol. Soc.*, *125*(554), 723–757, ISSN:1477-870X.

Greybush, S. J., E. Kalnay, T. Miyoshi, K. Ide, M. J. Hoffman, J. Eluszkiewicz, R. Hoffman, and R. J. Wilson (2011), Martian atmosphere data assimilation of TES and MCS retrievals, paper presented at the Fourth International Workshop on the Mars Atmosphere: Modelling and Observations, CNES, Paris, 8–11 February.

Guo, X., W. Lawson, M. I. Richardson, and A. D. Toigo (2009), Fitting the Viking lander surface pressure cycle with a Mars general circulation model, *J. Geophys. Res.*, *114*(E7), E07006, doi:10.1029/2008JE003302.

Heavens, N. G., M. I. Richardson, A. Kleinböhl, D. M. Kass, D. J. McCleese, W. Abdou, J. L. Benson, J. T. Schofield, J. H. Shirley, and P. M. Wolkenberg (2011a), The vertical distribution of dust in the Martian atmosphere during northern spring and summer: Observations by the Mars Climate Sounder and analysis of zonal average vertical dust profiles, *J. Geophys. Res.*, *116*, E04003, doi:10.1029/2010JE003691.

Heavens, N. G., M. I. Richardson, A. Kleinböhl, D. M. Kass, D. J. McCleese, W. Abdou, J. L. Benson, J. T. Schofield, J. H. Shirley, and P. M. Wolkenberg (2011b), Vertical distribution of dust in the Martian atmosphere during northern spring and summer: High-altitude tropical dust maximum at northern summer solstice, *J. Geophys. Res.*, *116*, E01007, doi:10.1029/2010JE003692.

Hoffman, M. J., S. J. Greybush, E. Kalnay, R. N. Hoffman, J. Eluszkiewicz, T. Miyoshi, K. Ide, and R. J. Wilson (2010a), Ensemble Kalman filter data assimilation of TES retrievals, *Bull. Am. Astron. Soc.*, *42*, 1042.

Hoffman, M. J., S. J. Greybush, R. J. Wilson, G. Gyarmati, R. N. Hoffman, E. Kalnay, K. Ide, E. J. Kostelich, T. Miyoshi, and I. Szunyogh (2010b), An ensemble Kalman filter data assimilation system for the Martian atmosphere: Implementation and simulation experiments, *Icarus*, *209*(2), 470–481.

Houben, H. (1999), Assimilation of Mars global surveyor meteorological data, *Adv. Space Res.*, *23*(11), 1899–1902.

Houtekamer, P. L., and H. L. Mitchell (2006), Ensemble Kalman filtering, *Q. J. R. Meteorol. Soc.*, *131*(613), 3269–3289.

Inada, A., M. I. Richardson, M. A. Mischna, C. E. Newman, A. D. Toigo, and A. R. Vasavada (2005), Simulation of water cycle with a Martian weather research and forecast model, *Eos Trans. AGU*, *86*(52), Fall Meet. Suppl., Abstract P21E-08.

Johnson, S. S., M. A. Mischna, T. L. Grove, and M. T. Zuber (2008), Sulfur-induced greenhouse warming on early Mars, *J. Geophys. Res.*, *113*, E08005, doi:10.1029/2007JE002962.

Kahre, M. A., R. J. Wilson, J. L. Hollingsworth, and R. M. Haberle (2010), Using assimilation techniques to model Mars' dust cycle with the NASA Ames and NOAA/GFDL Mars general circulation models, *Bull. Am. Astron. Soc.*, *42*, 1031.

Kalman, R. (1960), A new approach to linear filtering and prediction problems. *J. Basic Eng.*, *82*(1), 35–45.

Kalman, R., and R. Bucy (1961), New results in linear filtering and prediction theory, *J. Basic Eng.*, *83*(3), 95–108.

Kalnay, E. (2002), *Atmospheric Modeling, Data Assimilation and Predictability*, Cambridge Univ. Press, Cambridge, U. K.

Kalnay, E. (2009), Ensemble Kalman filter: Current status and potential, in *Data Assimilation: Making Sense of Observations*, pp. 69–92, Springer, Berlin.

Lacis, A., and V. Oinas (1989), A description of the correlated *k* distribution method for modeling nongray gaseous absorption, thermal emission, and multiple scattering in vertically inhomogeneous atmospheres, *J. Geophys. Res.*, *96*(D5), 9027–9063.

Lee, C., et al. (2009), Thermal tides in the Martian middle atmosphere as seen by the Mars Climate Sounder, *J. Geophys. Res.*, *114*, E03005, doi:10.1029/2008JE003285.

Lewis, S. R., and P. L. Read (1995), An operational data assimilation scheme for the martian atmosphere. *Adv. Space Res.*, *16*(6), 9–13.

Lewis, S. R., M. Collins, P. L. Read, F. Forget, F. Hourdin, R. Fournier, C. Hourdin, O. Talagrand, and J.-P. Huot (1999), A climate database for Mars, *J. Geophys. Res.*, *104*(E10), 24,177–24,194.

Lewis, S. R., P. L. Read, B. J. Conrath, J. C. Pearl, and M. D. Smith (2007), Assimilation of thermal emission spectrometer atmospheric data during the Mars Global Surveyor aerobraking period, *Icarus*, *192*(2), 327–347.

Lorenc, A. C., R. S. Bell, and B. Macpherson (1991), The meteorological-office analysis correction data assimilation scheme, *Q. J. R. Meteorol. Soc.*, *117*, 59–89.

McCleese, D. J., J. T. Schofield, F. W. Taylor, S. B. Calcutt, M. C. Foote, D. M. Kass, C. B. Leovy, D. A. Paige, P. L. Read, and R. W. Zurek (2007), Mars Climate Sounder: An investigation of thermal and water vapor structure, dust and condensate distributions in the atmosphere, and energy balance of the polar regions, *J. Geophys. Res.*, *112*, E05S06, doi:10.1029/2006JE002790.

Mischna, M. A., M. I. Richardson, C. E. Newman, A. D. Toigo, A. R. Vasavada, and A. Inada (2005), Orbitally-driven change in the Martian atmosphere, *Eos Trans. AGU*, *86*(52), Fall Meet. Suppl., Abstract P31B-0202.

Mischna, M. A., A. D. Toigo, C. E. Newman, and M. I. Richardson (2006), Development of a new global, scalable and generic general circulation model for studies of the Martian atmosphere, paper presented at the Second Workshop on Mars Atmosphere Modelling and Observations, Granada, Spain, CNES, 27 February to 3 March.

Montabone, L., S. R. Lewis, P. L. Read, and D. P. Hinson (2006), Validation of Martian meteorological data assimilation for MGS/TES using radio occulation measurements, *Icarus*, *185*, 113–132.

Moudden, Y., and J. M. Forbes (2010), Data assimilation applied to Mars Climate Sounder observations, Abstract P51E-08 presented at 2010 Fall Meeting, AGU, San Francisco, Calif., 13–17 Dec.

Newman, C., P. Read, and S. Lewis (2004), Investigating atmospheric predictability on Mars using breeding vectors in a general-circulation model, *Q. J. R. Meteorol. Soc.*, *130*(603) 2971–2989, ISSN:1477-870X.

Newman, C. E., M. I. Richardson, and A. D. Toigo (2006), Modeling the Martian dust cycle with MarsWRF, *Eos Trans. AGU*, *87*(52), Fall Meet. Suppl., Abstract P23A-0048.

Richardson, M. I., A. D. Toigo, and C. E. Newman (2007), PlanetWRF: A general purpose, local to global numerical model for planetary atmospheric and climate dynamics, *J. Geophys. Res.*, *112*, E09001, doi:10.1029/2006JE002825.

Rodgers, C. D., and B. J. Connor (2003), Intercomparison of remote sounding instruments, *J. Geophys. Res.*, *108*(D3), 4116, doi:10.1029/2002JD002299.

Skamarock, W. C., and J. B. Klemp (2008), A time-split non-hydrostatic atmospheric model for weather research and forecasting applications, *J. Comp. Phys.*, *227*(7), 3465–3485.

Smith, M., J. Pearl, B. Conrath, and P. Christensen (2001), Thermal Emission Spectrometer results: Mars atmospheric thermal structure and aerosol distribution, *J. Geophys. Res.*, *106*(E10), 23,929–23,945.

Soto, A., and M. I. Richardson (2009), Water at the surface of Mars, in *Second Workshop on Mars Valley Networks*, pp. 66–68, Smithsonian Inst., Washington, D. C.

Stensrud, D. J. (2007), *Parameterization Schemes: Keys to Understanding Numerical Weather Prediction Models*, 459 pp., Cambridge Univ. Press, Cambridge, U. K.

Wilson, R. J., S. R. Lewis, L. Montabone, and M. D. Smith (2008), Influence of water ice clouds on Martian tropical atmospheric temperatures, *Geophys. Res. Lett.*, *35*, L07202, doi:10.1029/2007GL032405.

Wolff, M. J., and R. T. Clancy (2003), Constraints on the size of Martian aerosols from Thermal Emission Spectrometer observations *J. Geophys. Res.*, *108*(E9), 5097, doi:10.1029/2003JE002057.

J. L. Anderson, N. Collins, and T. Hoar, IMAGe, NCAR, PO Box 3000, Boulder, CO 80307, USA.

W. G. Lawson, Point Carbon, 1200 First Street NE, Ste. 310, Washington, DC 20002, USA.

C. Lee and M. I. Richardson, Ashima Research, 600 S. Lake Ave., Ste. 104, Pasadena, CA 91101, USA. (lee@ashimaresearch.com)

M. Mischna, Jet Propulsion Laboratory, Pasadena, CA 91109, USA.